Formation of crownlike and related nanostructures on thin supported gold films irradiated by single diffraction-limited nanosecond laser pulses

Yu. N. Kulchin,[1,2] O. B. Vitrik,[1,2] A. A. Kuchmizhak,[1,*] V. I. Emel'yanov,[3] A. A. Ionin,[4] S. I. Kudryashov,[4,5,†] and S. V. Makarov[4]

[1]*Institute of Automation and Control Processes, Far Eastern Branch, Russian Academy of Science, 690041 Vladivostok, Russia*

[2]*Far-Eastern Federal University, 690041 Vladivostok, Russia*

[3]*Moscow State University, 119899 Moscow, Russia*

[4]*P. N. Lebedev Physical Institute, Russian Academy of Science, 119991 Moscow, Russia*

[5]*National Research Nuclear University MEPhI (Moscow Engineering Physics Institute), 115409 Moscow, Russia*

(Received 8 April 2014; revised manuscript received 18 July 2014; published 26 August 2014)

A type of laser-induced surface relief nanostructure—the nanocrown—on thin metallic films was studied both experimentally and theoretically. The nanocrowns, representing a thin corrugated rim of resolidified melt and resembling well-known impact-induced water-crown splashes, were produced by single diffraction-limited nanosecond laser pulses on thin gold films of variable thickness on low-melting copper and high-melting tungsten substrates, providing different transient melting and adhesion conditions for these films. The proposed model of the nanocrown formation, based on a hydrodynamical (thermocapillary Marangoni) surface instability and described by a Kuramoto-Sivashinsky equation, envisions key steps of the nanocrown appearance and gives qualitative predictions of the acquired nanocrown parameters.

DOI: 10.1103/PhysRevE.90.023017 PACS number(s): 47.20.Ma, 47.61.−k, 79.20.Eb

I. INTRODUCTION

Direct laser nanostructuring of thin metallic films appears as a versatile large-scale technology in fabricating nanophotonic and plasmonic elements and devices [1]. Single tightly focused short and ultrashort laser pulses are used to fabricate in a deterministic "bottom-up" way different types of single-element nanostructures—localized microbumps [2,3], nanojets [4–6], nanoholes [7–10], or nanoparticles [11], as well as their regular arrays (see, e.g., [11]). Likewise, quasiregular arrays of nanotrenches [12,13] or microbumps (microcolumns) [14–16] were produced on macroscopic scales through various "top-down" processes by weakly focused multiple short and ultrashort laser pulses on material surfaces via relief self-organization, driven by diverse surface instabilities of transient surface molten layers [17,18]. Similar phenomena were observed upon weak laser focusing onto nanoscale metallic lines [19] or rings [20], resulting in nanoparticle ensembles via developing hydrodynamic instabilities.

Recently, an unusual type of laser-driven surface relief instability in the form of nanocrowns—quasiregularly modulated nanorims of laser-molten surface layers as a sequence of nanotips with beads atop—were observed upon single-shot irradiation of a thin gold film deposited on a Si substrate by strongly focused femtosecond laser pulses [21]. The shape of the micron-wide crown observed in Ref. [21] is typical for well-known fluid crowns formed by impact of a symmetric object onto a fluid surface and can be arbitrarily related either to Rayleigh-Plateau, Rayleigh-Taylor, or Richtmyer-Meshkov hydrodynamic (HD) instabilities [22,23]. Such surface crownlike relief with numerous spikes was shown to appear at the initial surface instability stage, while the top beads emerge at a more developed nonlinear stage (see Fig. 3 in Ref. [23]). Moreover, these surface impact-driven relief instabilities can be potentially identified in term of Reynolds (Re) and Weber (We) numbers as different regions—Pelegrine sheet, crown splash, microdroplet splash, and intermediate cases—of a unified Re-We phase diagram [22,23]. In contrast, laser-driven melt instabilities exhibit much more complex, "bulk" character for the three-dimensional transient temperature and stress gradients and thus require more profound phenomenological investigation and more complicated, different theoretical modeling.

In this work, we report on the observation of diverse surface nanocrowns and related surface nanostructures on 25- and 50-nm-thick supported Au/Pd films on a bulk low-melting Cu substrate at variable energies of incident single *nanosecond* diffraction-limited laser pulses, in comparison with a 50-nm-thick supported Au/Pd film on a bulk high-melting W (a refractory metal) substrate demonstrating just smooth rims. These frozen surface topologies are qualitatively enlightened in the framework of our theoretical model of a hydrodynamic instability of laser-melted surface appearance.

II. EXPERIMENTAL SETUP AND PROCEDURES

In our experiments we used 25- and 50-nm-thick Au/Pd (80/20 wt %) alloy films deposited by magnetron sputtering (Quorum Technologies) either on a smooth (rms ∼3 nm) edge of a cut Cu wire, or on a W substrate, both prepolished by accelerated Ag^+ ions (Hitachi IM4000). Linearly polarized second-harmonic ($\lambda = 532$ nm) pulses of a Nd:YAG laser (Solar LS LQ215) with a pulse width $\tau_p \approx 7$ ns [full width at half maximum (FWHM)] and a maximum energy $E \leq 10$ mJ (TEM_{00} mode) were used for surface nanostructuring.

Each p-polarized laser pulse was focused onto the Au/Pd film (Fig. 1) by means of an apertureless dielectric probe (ADP), a tapered 20-mm-long section of a single-mode optical fiber (Thorlabs SM400) with a constant taper angle

*ku4mijak@mail.dvo.ru
†sikudr@sci.lebedev.ru

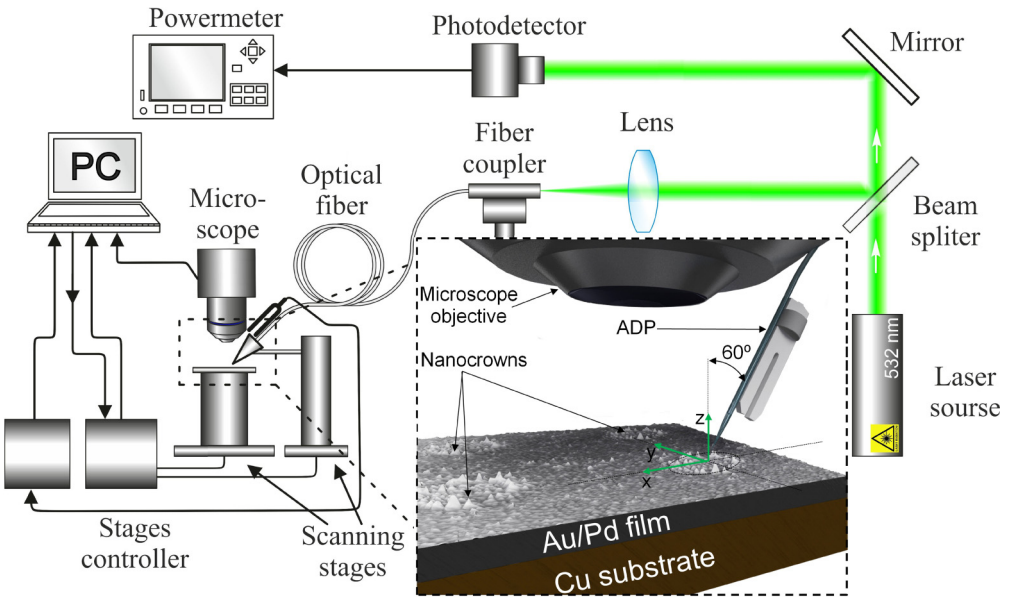

FIG. 1. (Color online) Experimental setup for surface nanostructuring.

~12° [9,10]. Such ADP provides spatial filtering and focusing of a laser beam, resulting in a diffraction-limited output spot ($R_{1/e} \approx 0.3$ μm at the normal incidence) with a nearly Gaussian spatial profile and relatively deep focal depth ($\sim\lambda/2$) [9,10]. The laser pulses were effectively coupled to the ADP using a fiber coupler (Thorlabs MBT612D/M). During laser nanostructuring, the ADP tip was located 50 nm above the sample surface and inclined at an angle of 60° (inset in Fig. 1) to the sample surface normal, yielding an elliptical Gaussian spot with $R_{x,1/e} \approx 0.65$ μm and $R_{y,1/e} \approx 0.4$ μm. The probe-to-sample distance was controlled using the tuning fork feedback. Visual control of the ADP motion and the Au/Pd film damage was performed by means of a high-resolution optical microscope Hirox KH7700 (optical magnification, 700×–7000×; working distance ≈ 3.4 mm).

The laser pulse energy entering the fiber was varied using a polarizing attenuator. To measure the pulse energy E at the ADP tip, the output laser radiation was collected by a microscope objective [numerical aperture (NA) = 0.65] and focused on the photodetector (J-10SI-HE energy sensor, Coherent EPM2000). Surface topology of the laser-structured Au/Pd film was characterized using an atomic force microscope (AFM) (NanoDST Pacific Nanotechnology) in the close-contact mode with ultrathin Au-coated cantilevers (NT MDT 01_DLC and NSC05_10°). All experiments were performed under ambient conditions.

III. EXPERIMENTAL RESULTS

A. 50- and 25-nm-thick Au/Pd films on Cu substrates

Typical submicron-scale structures, emerging on the surface of the 50-nm-thick Au/Pd film upon single-shot laser irradiation, are shown by AFM images in Figs. 2(a)–2(c). The minimal surface modification appears at $E \approx 1.9$ nJ [Fig. 2(a)], referred to here as "nanocrown." It exhibits a set of sub-100-nm-wide and sub-30-nm-high major nanotips, connected by a series of less pronounced minor nanotips, arranged altogether in the form of a slightly elliptical modulated rim with major and minor semiaxes ratio $b^{\text{crown}} = R_x/R_y \approx 1.8$ [Fig. 2(a)]. This ratio b^{crown} represents the oblique incidence of the laser radiation in this ADP focusing geometry (Fig. 1, inset). The nanocrown radii monotonously increase with the increasing pulse energy E [Figs. 2(b), 2(c), and 3]. The total number of the constituent major and minor nanotips $N_m \sim 10 - 10^2$, with their characteristic dimensions remaining almost constant versus increasing E [Figs. 2(a)–2(c)].

At higher energies, $E \approx 2.7$ nJ and $E \approx 5.5$ nJ, other known types of surface structures—submicron bumps and holes—appear on the film surface in the laser spot center [Figs. 2(d) and 2(f)], while the peripheral nanocrowns

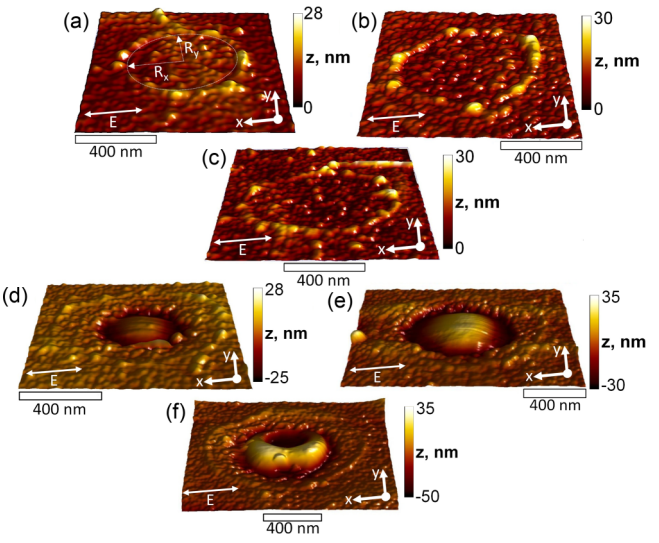

FIG. 2. (Color online) (a)–(f) AFM images of the laser-induced surface structures in the 50-nm-thick Au/Pd film on the Cu substrate at laser energies $E \approx 1.9$ (a), 2.15 (b), 2.3 (c), 2.7 (d), 4.9 (e), and 5.5 nJ (f).

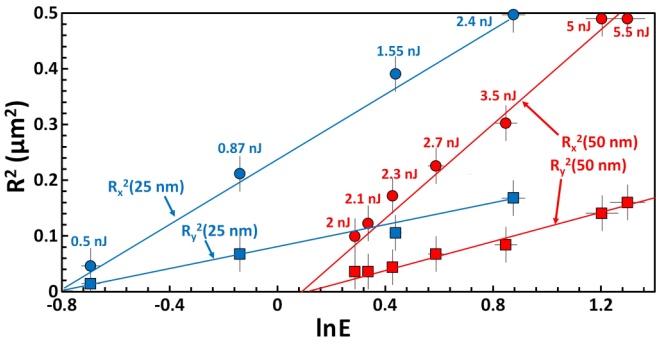

FIG. 3. (Color online) Squared radii of x and y semiaxes of nanocrowns versus $\ln E$ on the 25-nm-thick (blue symbols) and 50-nm-thick (red symbols) gold films on the Cu substrates. The straight lines fit the experimental data using the functions $R^2_{x,y} = \Delta^2_{x,y} \ln(E/E_c)$, where $\Delta_{x,y}$ are the characteristic lateral scales of laser energy deposition.

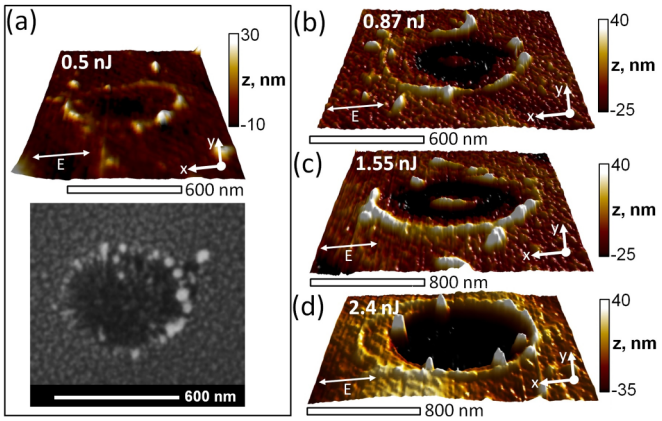

FIG. 4. (Color online) AFM and SEM images of the laser-induced surface structures in the 25-nm-thick Au/Pd film on the Cu substrate at laser energies $E \approx 0.5$ (a), 0.87 (b), 1.55 (c), and 2.4 nJ (d).

become less prominent. Single-shot-driven growth of such bumps and holes is enhanced at the increasing laser energy [Figs. 2(d)–2(f)], being accompanied by partial displacement of the film material to form the local submicron depressions and bumps. In contrast, the surface level in the vicinity of the observed nanocrowns remains constant [Figs. 2(a)–2(c)], while the detailed AFM analysis indicates simultaneously the increased grain size inside the film region surrounded by the nanocrown rim, apparently, following laser-induced melting and resolidification processes within the focal spot.

For the Gaussian intensity distribution in the focal laser spot [9,10], the experimental dependences of R^2_x and R^2_y on E (Fig. 3) can be fitted in the form $R^2_{x,y} = \Delta^2_{x,y} \ln E/E_c$, where E_c is the threshold energy of the nanocrown formation, and $\Delta_{x,y}$ (50 nm) are the characteristic lateral scales of laser energy deposition [24], including the focal spot size and the heat transport length. The resulting two characteristic scales of the transient surface modification, $\Delta_x(50\text{ nm}) \approx 0.63 \pm 0.01\ \mu$m and $\Delta_y(50\text{ nm}) \approx 0.35 \pm 0.01\ \mu$m, with their ratio $\Delta_x/\Delta_y \approx 1.8$, are consistent with the magnitude $b^{\text{crown}} \approx 1.8$. In comparison to the same focusing scales $R_{x,1/e} \approx 0.65\ \mu$m and $R_{y,1/e} \approx 0.4\ \mu$m, the good correspondence of $R_{x,1/e}$ ($R_{y,1/e}$) and Δ_x (Δ_y) magnitudes indicates the presumable vertical heat conduction into the bulk copper substrate. The threshold fluence of the nanocrown formation, $F_c = E_c/(\pi \Delta_x \Delta_y)$, was obtained by extrapolating the dependences to $R^2_{x,y} = 0$, yielding the threshold energy $E_c(50\text{ nm}) \approx 1.1 \pm 0.1$ nJ and the corresponding threshold fluence $F_c(50\text{ nm}) \approx 0.16 \pm 0.02$ J/cm^2.

Likewise, the 25-nm-thick Au/Pd film on the Cu substrate demonstrates a number of similar crownlike structures around the single-shot craters, becoming more pronounced for the increasing pulse energy E (Fig. 4). Meanwhile, for the thinner film the fitted parameters $\Delta_x(25\text{ nm}) = 0.54\ \mu$m and $\Delta_y(25\text{ nm}) = 0.313\ \mu$m ($\Delta_x/\Delta_y = 1.72$) are somewhat smaller, than for the thicker film, while the corresponding threshold energy $E_c(25\text{ nm}) \approx 0.45 \pm 0.07$ nJ is almost two times lower. As a result, the crown-formation threshold fluence $F_c \approx 0.09 \pm 0.02$ J/cm^2 for the 25-nm-thick film is consistently scalable with the film thickness, accounting for the higher threshold $F_c(50\text{ nm}) \approx 0.16 \pm 0.02$ J/cm^2 for the thicker film.

B. 50-nm-thick Au/Pd film on W substrate

In contrast with the evident crown formation on the 25- and 50-nm-thick Au/Pd films on the Cu substrates, a 50-nm-thick Au/Pd film on a tungsten substrate demonstrates a number of smooth asymmetric rims of variable, energy-dependent heights right around the single-shot craters (Fig. 5). Moreover, both increased rim heights and diameters are observed at the same focusing conditions and comparable pulse energies (cf. Figs. 2, 4, and 5). Comparing to the 50-nm-thick Au/Pd film on the Cu substrate, in this case the experimental dependences R^2_x and R^2_y versus E in Fig. 5 exhibit significantly larger energy deposition spatial scales $-\Delta_x \approx 0.83 \pm 0.01\ \mu$m and $\Delta_y \approx 0.51 \pm 0.01\ \mu$m ($\Delta x/\Delta_y \approx 1.62$), corresponding to significantly higher threshold energy $E_c \approx 1.9 \pm 0.1$ nJ, but

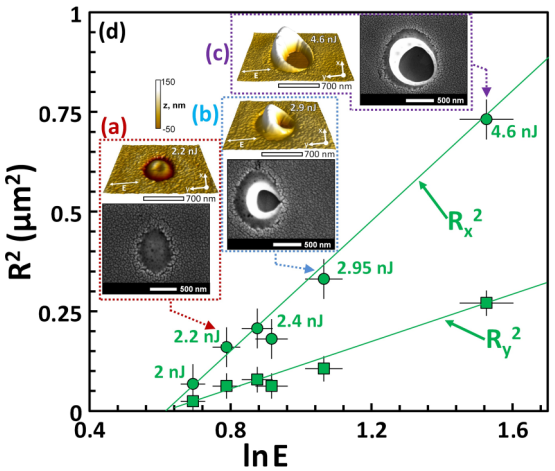

FIG. 5. (Color online) (a)–(c) Pairs of AFM and SEM images of the laser-induced surface structures (nanorims and nanocraters) in the 50-nm-thick Au/Pd film on a tungsten substrate at the laser energies $E \approx 2.2$ (a), 2.9 (b), and 4.6 nJ (c). (d) Squared radii of x and y semiaxes of the rims versus $\ln E$.

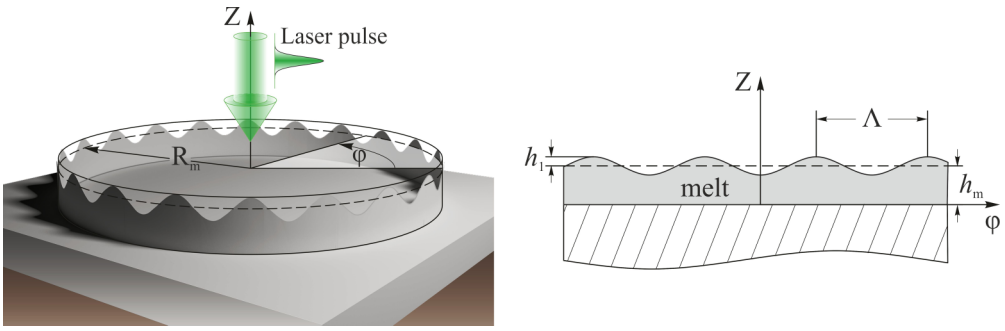

FIG. 6. (Color online) (a) Sketch of a molten pool with the rim of the radius R_m and the periodically (azimuthally) modulated height $h = h_m + h_1$ (the nanocrown). (b) Angular fragment of the nanocrown shown in (a), which illustrates the height modulation of the molten rim with the small amplitude h_1 ($h_1 \gg h_m$) and the wavelength Λ.

somewhat lower threshold fluence $F_c \approx 0.13 \pm 0.02$ J/cm^2 for nanorim formation in the film on the W substrate.

IV. HYDRODYNAMIC MODEL OF NANOCROWN FORMATION

To envision the essential physics behind the nanocrown-formation mechanism, a two-stage hydrodynamic model was developed to describe the underlying instability of the molten surface.

A. First stage: Formation of a molten cylindrical rim on surface

The 7-ns 532-nm laser pulse with the Gaussian intensity distribution (the focal radius $R_{1/e}$) melts a surface layer of the thin gold film and the copper substrate within the radius R_m to depth H_m, which is a decreasing radial function $H_m = H_m(|\boldsymbol{r}|)$ in the surface plane, with $H_m(R_m) = 0$. Surface temperature in the center of the melt pool is higher than that at its periphery, resulting in the gradient of its surface tension σ directed outward due to $\partial s/\partial T < 0$ for liquid metals [25], and pulling the molten surface layer away from the spot center to its periphery. Moreover, friction forces in the melt layer are increased versus its radially decreasing depth, slowing down the outward melt motion and eventually stopping it at the melt-solid boundary at $r = R_m$, where the thermocapillary pressure forces push it to move up along the surface normal. Such complex motion within the melt pool yields a cylindrical rim as a thin wall of the molten gold and copper with radius R_m and height h [Fig. 6(a)].

To describe subsequent evolution of the cylindrical rim up to its total solidification, one should analyze the influence of other factors. First, the temperature gradient in the rim wall is directed from its top to the bottom ($\partial T/\partial z < 0$), since the lower part of the wall is formed by flow of the hotter molten material from the spot center, while the upper part of the wall appears through displacement of the cooler peripheral melt. Second, a perturbation of the molten rim height h leads to a modulation of surface tension: $\nabla\sigma = -|\partial\sigma/\partial T|(\partial T/\partial z)\nabla h$. In this case, directions of liquid flows at each tip depend on the direction of the temperature gradient ($\partial T/\partial z$) in the cylinder wall along its height. Therefore, in the case of such negative temperature gradient, $(\partial T/\partial z) < 0$, thermocapillary forces provide a HD instability of the wall relief for $\nabla\sigma \sim \nabla h$.

B. Second stage: Marangoni hydrodynamic instability of the cylindrical rim height

The height of the molten cylindrical rim in Fig. 6(b) can be written in the form $h = h_m + h_1(\boldsymbol{r},t)$, where h_0 is the spatially uniform height and $h_1(\boldsymbol{r},t)$ is the small spatially nonuniform perturbation ($h_1 \ll h_m$) of the rim height, arising from the development of the thermocapillary (Marangoni) HD instability. The HD thermocapillary-induced modulation of the thickness of the viscous molten layer can be described, in the long-wave limit ($2\pi h_1/\Lambda \ll 1$), by the two-dimensional hydrodynamic Kuramoto-Sivashinsky (HDKS) equation for $h_1(\boldsymbol{r},t)$ [18]:

$$\frac{\partial h_1}{\partial t} = -D\Delta h_1 - D_1 l_\parallel^2 \Delta^2 h_1 - \frac{2D}{h_m}(\nabla h_1)^2, \qquad (1)$$

where $D = (|\sigma_T| h_m^2/2\rho\eta)|\partial T/\partial z|_{h_m}$; $(\partial T/\partial z)_{h_m} \equiv (\partial T/\partial z)_{z=h_m}$ is the normal temperature gradient at the tip of the melted spot rim; $|\sigma_T| = |\partial\sigma/\partial T|$; ρ and η are the melt density and kinematic viscosity, respectively; $D_1 = \sigma h_m/3\rho\eta$; and the scaling parameter $l_\parallel = h_m/\sqrt{3}$. Above, Δ and ∇ are the two-dimensional Laplace and gradient operators, respectively. The HDKS equation (1) was earlier derived in [18] from a more general HD equation given in [26].

We assume the thickness of the rim wall $\Delta R_m \ll R_m$ and consider one-dimensional HD instability of the rim with the radius R_m. In this case, the cylindrical rim height depends on the angle between x or y axis, and the vector $\boldsymbol{r}$ [see Fig. 4(a)]: $h = h_m + h_1(\varphi,t)$. Then, one can transform Eq. (1) to the HDKS equation on the ring,

$$\frac{\partial h_1}{\partial t} = -\Omega\frac{\partial^2 h_1}{\partial\varphi^2} - \Omega b^2\frac{\partial^4 h_1}{\partial\varphi^4} - \frac{2\Omega}{h_m}\left(\frac{\partial h_1}{\partial\varphi}\right)^2, \qquad (2)$$

where $\Omega = D/R_m^2$ and $b^2 = D_1 l_\parallel^2/DR_m^2$.

To carry out linear analysis of the HD instability of the molten cylindrical rim height, the solution of the linearized Eq. (2) was written as

$$h_1(\varphi,t) = \sum_N h_{10}(N)\exp(iN\varphi + \lambda_N t), \qquad (3)$$

where $h_{10} \equiv$ const, N is an integer, and λ_N is the growth rate,

$$\lambda_N = \Omega N^2 - \Omega b^2 N^4, \qquad (4)$$

for the Nth azimuthal harmonic. The solution in the form of Eq. (3) satisfies the periodical condition on the ring $h_1(\varphi,t) = h_1(\varphi + 2\pi,t)$.

From the analysis of Eq. (4), one can find the maximum growth rate at

$$N = N_m = \sqrt{\frac{D}{2D_1}}\frac{R_m}{l_\parallel}. \quad (5)$$

Thus, the wavelength of the dominant rim height modulation reads

$$\Lambda_m = \frac{2\pi R_m}{N_m} = \frac{4\pi}{3}h_m\left[\frac{\sigma}{|\sigma_T|\,|\partial T/\partial z|_{h_m}\,h_m}\right]^{1/2}. \quad (6)$$

The cylindrical rim height modulation [Fig. 6(b)] leads to formation of the crown structure [Fig. 6(a)]. The tip number in the crown, according to Eq. (5), equals

$$N_m = \frac{3R_m}{2h_m}\left[\frac{|\sigma_T|\,|\partial T/\partial z|_{h_m}\,h_m}{\sigma}\right]^{1/2}, \quad (7)$$

and the growth rate of the dominant modulation is given by

$$\lambda_{\max} = \left(\frac{D^2}{4D_1}\right)\frac{1}{l_\parallel^2} = \frac{9\sigma}{16\rho\eta h_m}\left(\frac{|\partial T/\partial z|_{h_m}\,|\sigma_T|\,h_m}{\sigma}\right)^2. \quad (8)$$

V. DISCUSSION

In our experiments on the Cu-supported gold films, there are prominent indications of the increased nanograin sizes within the observed nanocrowns, which can be related to the film annealing—melting and resolidification—processes (e.g., the Cu melting temperature $T_m \approx 1356$ K, the melting enthalpy $\Delta H_m \approx 13$ kJ/mole [27], the Au melting temperature $T_m \approx 1337$ K [28], and the Pd melting temperature $T_m \approx 1825$ K [29]). The related transient surface melt thickness, which is the key parameter for the crown-formation process, was evaluated using [30]

$$h_m \approx \sqrt{4\chi\tau_p}\ln(F/F_m), \quad (9)$$

where the characteristic heat conduction length $\sqrt{4\chi\tau_p} \approx 1.7$ μm for the known high-temperature thermal diffusivity in copper, χ (1000 K) ≈ 1 cm^2/s [27] (cf. the penetration depth in gold at 532 nm ≈ 17 nm [31]), and the melting threshold $F_m \leqslant F_c \approx 0.22$ J/cm^2. Then, for $\ln(F/F_m) \leqslant 1$, the submicron-deep melt pool may appear on the Cu surface in each laser shot prior to the nanocrown formation. In contrast, melting of W occurs at much (almost three times) higher $T_m \approx 3693$ K and $\Delta H_m \approx 35.1$ kJ/mole [27], thus requiring much higher thermal fluxes (laser fluences) at the rather comparable high-temperature thermal diffusivity χ (1000 K) ≈ 0.4 cm^2/s [27]. Hence, in this work at comparable incident laser fluences the W substrate may remain solid, carrying the rather thin ($\approx$ 50-nm-thick) molten Au/Pd layer, in comparison to $h_m \sim 10^{-5}$–10^{-4} cm for the above-mentioned Cu-supported gold films.

The developed HD model provides basic understanding of nanocrown formation on a molten film-substrate surface and some useful estimates of its evident and "hidden" characteristics. For numerical estimates of the number of nanoridges in the nanocrown, we use in Eq. (7) experimental values $h_m \sim 10^{-5}$–10^{-4} cm for the Cu-supported gold films and $\sim 10^{-5}$ cm for the W-supported gold films, respectively, and $R_m \sim \Delta_{x,y} \sim 5 \times 10^{-5}$ cm. Several approximations in Eq. (7) were also taken, assuming $|\partial T/\partial z|_{h_m} \sim T/h_m$ and $|\sigma_T| \sim \sigma/T$, to simplify Eq. (7) to $N \approx 3R_m/2h_m$. Thus, we estimate the number of nanoridges as $N \sim 10$ for the Cu-supported gold films in agreement with the experimental numbers of the major tips with the typical spacings $\Lambda \sim 10^{-5}$ cm (Figs. 2 and 4). In contrast, a much thinner ($h_m \sim 10^{-5}$ cm) molten layer is expected for the W-supported gold films, resulting in accordance with Eqs. (6) and (7) in a much larger number of spikes ($N \sim 10^2$) and much smaller spacings $\Lambda \sim 10^{-6}$ cm. Apparently, such closely spaced, tiny nanotips can hardly be resolved by AFM, accounting also for the finite tip widths, and thus may appear as continuous rims.

Furthermore, to derive the important relationship between N_m and E, one can assume that during the laser pulse width the surface molten ring sheet of a thickness δ and the width $L = V_r\tau_p$ (V_r is the characteristic radial melt flow velocity) is displaced from the periphery region of the molten circle spot of the radius R_m to form the rim with the same thickness δ and the height h_m (here, the circular shape of the molten spot is assumed for simplicity). The volume of this ring sheet is $2\pi R_m L\delta$. The radial flow velocity $V \sim \partial T/\partial r$, where the lateral temperature distribution is $T(r) = T_0\exp(-r^2/\Delta^2)$. At $r \sim R_m$, the characteristic radial velocity $V = \text{const}T_0R_m\exp(-R_m^2/\Delta^2)$ and from the volume conservation condition $2\pi R_m L\delta = 2\pi R_m h_m\delta$ one finds $h_m = \text{const}T_0R_m\exp(-R_m^2/\Delta^2)$. We use here $T_0 \sim E$, $R_m^2 = \Delta^2\ln E/E_c$ (see Figs. 4 and 6) to obtain $h_m = \text{const}\sqrt{\ln(E/E_c)}$. Thus, $N(E) \sim 3R_m/2h_m = \text{const}$ and is independent of the laser pulse energy. This conclusion corresponds to the whole energy interval of nanocrown formation [Figs. 2(a)–2(c)], in which the number of pronounced major nanotips is indeed independent of pulse energy, $N(E) \sim 10 = \text{const}$. Then, the appearance of a number of the minor tips with smaller spacings can be attributed to the second-harmonic generation (SHG) of rim height modulation, based on the last term $\sim (\partial h_1/\partial\varphi)^2$ in the HDKS equation (2) (cf. [32]). At higher pulse energies [Figs. 2(e) and 2(f)], the SHG can become the dominant process and is responsible for the formation of all nanocrown tips.

The nanocrown-formation time $t_{\text{form}} = \lambda_{\max}^{-1}$ can be estimated, using Eq. (8) and the molten copper parameters $\eta \approx 1 \times 10^{-3}$ Pa s and σ (1150 °C–1550 °C) ≈ 1.4 N/m [27], and the assumptions previously made. Then, the crown-formation time $t_{\text{form}} \sim 3.7$ ns $< \tau_p$, that corresponds to the increment factor $\lambda_{\max}\tau_p \sim 2$ in Eq. (3). After the laser pulse termination, the molten cylindrical rim becomes frozen in the surface promptly ($t_{\text{freeze}} \sim h_m^2/\chi \sim 0.1 - 1$ ns for χ (1000 K) ≈ 1 cm^2/s for copper [27]), resulting in the solidified nanocrown.

Interestingly, the main difference between the nanocrowns formed by femtosecond [21] and nanosecond (our experiments) laser irradiation is the shape of the corrugated wall. In the case of femtosecond laser action, each nanocrown maximum looks as a nanotip with a bead atop, while in our experiments formation of only the tiplike corrugations was observed, yielding from either Rayleigh-Plateau, Rayleigh-

Taylor, or Richtmyer-Meshkov instabilities [22,23]. These two characteristic shapes of crowns were shown to appear at different stages of the HD surface instability with formation of ridges at the initial stage and spikes with tip bead at a more developed nonlinear stage (see Fig. 3 in [23]). We believe that this explanation of crown shape differences can be also used in the case of laser-induced nanocrown formation in surface melts. However, in our specific case (no impact), another, Marangoni type of HD instability is assumed to play the key role in the nanocrown formation.

Finally, sub-100-nm through holes and nanobumps emerging at higher laser pulse energies appear as different surface topography features inside the nanocrowns on the metallic substrates, as compared to the same conditions of laser irradiation of a Au/Pd film deposited on quartz substrates [1–3], exhibiting substantially lower thermal conductivity and lower surface energy. In particular, in our case the different laser-induced topographies on the Au/Pd film can be ascribed to its stronger adhesion to the copper or tungsten substrates and Marangoni-like HD instability of the melt pool.

VI. CONCLUSIONS

In conclusion, an interesting type of laser-induced surface relief nanostructure on thin metallic films—the nanocrown—was studied both experimentally and theoretically. The nanocrowns were produced by single diffraction-limited nanosecond laser pulses on thin gold-palladium alloy films of variable thickness supported only by low-melting copper, but not high-melting tungsten substrates. The nanocrowns represent a thin corrugated wall, resembling well-known impact water-crown splashes. The proposed model based on the underlying hydrodynamical (thermocapillary Marangoni) surface instability, described by a hydrodynamical Kuramoto-Sivashinsky equation, throws light on the nanocrown-formation mechanism and gives reasonable predictions of the acquired nanocrown parameters.

Note added. As an illustration of the universal character of this instability, pronounced microcrowns were recently seeded and developed on silicon surfaces in a multishot ($1–10^3$ shots) regime both by IR (1030 nm) and visible (515 nm) femtosecond laser pulses [33].

ACKNOWLEDGMENTS

The authors from IACP acknowledge partial support from the Russian Foundation for Basic Research (Projects No. 13-02-00648-a, No. 14-02-31323-mol_a, No. 14-02-00205-a, and No. 14-02-31558-mol_a) and from Far Eastern Branch of RAS (Projects No. 12-02-P24-07 and No. 13-NTP-I-05). At LPI this work was supported by the RFBR grants (Grants No. 13-02-00971 and No. 14-32-50026) and the grants of the RAS Presidium Program No. 24 on nanotechnology.

[1] T. C. Chong, M. H. Hong, and L. P. Shi, Laser Photon. Rev. **4**, 123 (2010).
[2] F. Korte, J. Koch, and B. N. Chichkov, Appl. Phys. A **79**, 879 (2004).
[3] Y. Nakata, N. Miyanaga, and T. Okada, Appl. Surf. Sci. **253**, 6555 (2007).
[4] A. I. Kuznetsov, C. Unger, J. Koch, and B. N. Chichkov, Appl. Phys. A **106**, 479 (2012).
[5] J. P. Moening, S. S. Thanawala, and D. G. Georgiev, Appl. Phys. A **95**, 635 (2009).
[6] M. A. Gubko, W. Husinsky, A. A. Ionin, S. I. Kudryashov, S. V. Makarov, C. S. R. Nathala, A. A. Rudenko, L. V. Seleznev, D. V. Sinitsyn, and I. V. Treshin, Laser Phys. Lett. **11**, 065301 (2014).
[7] F. Korte, S. Adams, A. Egbert, C. Fallnich, A. Ostendorf, S. Nolte, M. Will, J.-P. Ruske, B. N. Chichkov, and A. Tünnermann, Opt. Express **7**, 41 (2000).
[8] F. Korte, J. Serbin, J. Koch, A. Egbert, C. Fallnich, A. Ostendorf, and B. N. Chichkov, Appl. Phys. A **77**, 229 (2003).
[9] Y. N. Kulchin, O. B. Vitrik, A. A. Kuchmizhak, A. V. Nepomnyashchii, A. G. Savchuk, A. A. Ionin, S. I. Kudryashov, and S. V. Makarov, Opt. Lett. **38**, 1452 (2013).
[10] A. A. Kuchmizhak, Y. N. Kulchin, O. B. Vitrik, A. G. Savchuk, S. V. Makarov, S. I. Kudryashov, and A. A. Ionin, Opt. Commun. **308**, 125 (2013).
[11] A. I. Kuznetsov, A. B. Evlyukhin, M. R. Gonçalves, C. Reinhardt, A. Koroleva, M. L. Arnedillo, R. Kiyan, O. Marti, and B. N. Chichkov, ACS Nano **5**, 4843 (2011).
[12] J. F. Young, J. S. Preston, H. M. van Driel, and J. E. Sipe, Phys. Rev. B **27**, 1155 (1983).
[13] E. V. Golosov, A. A. Ionin, Yu. R. Kolobov, S. I. Kudryashov, A. E. Ligachev, S. V. Makarov, Yu. N. Novoselov, L. V. Seleznev, D. V. Sinitsyn, and A. R. Sharipov, Phys. Rev. B **83**, 115426 (2011).
[14] S. I. Dolgaev, S. V. Lavrishev, A. A. Lyalin, A. V. Simakin, V. V. Voronov, and G. A. Shafeev, Appl. Phys. A **73**, 177 (2001).
[15] T. H. Her, R. J. Finlay, C. Wu, S. Deliwala, and E. Mazur, Appl. Phys. Lett. **73**, 1673 (1998).
[16] A. A. Ionin, S. I. Kudryashov, S. V. Makarov, A. A. Rudenko, L. V. Seleznev, D. V. Sinitsyn, E. V. Golosov, Y. R. Kolobov, and A. E. Ligachev, Appl. Phys. A **116**, 1133 (2014).
[17] D. W. Bäuerle, *Laser Processing and Chemistry* (Springer, Berlin, 2011).
[18] V. I. Emel'yanov, Laser Phys. **21**, 222 (2011).
[19] J. D. Fowlkes, L. Kondic, J. Diez, Y. Wu, and P. D. Rack, Nano Lett. **11**, 2478 (2011).
[20] Y. Wu, J. D. Fowlkes, P. D. Rack, J. A. Diez, and L. Kondic, Langmuir **26**, 11972 (2010).
[21] Y. Nakata, K. Tsuchida, N. Miyanaga, and H. Furusho, Appl. Surf. Sci. **255**, 9761 (2009).
[22] R. D. Deegan, P. Brunet, and J. Eggers, Nonlinearity **21**, C1 (2008).
[23] L. V. Zhang, P. Brunet, J. Eggers, and R. D. Deegan, Phys. Fluids **22**, 122105 (2010).
[24] J. M. Liu, Opt. Lett. **7**, 196 (1982).
[25] I. Egry, E. Ricci, R. Novakovic, and S. Ozawa, Adv. Colloid Interface Sci. **159**, 198 (2010).

[26] A. Oron, S. H. Davis, and S. G. Bankoff, Rev. Mod. Phys. **69**, 931 (1997).
[27] *Physical Quantities*, edited by I. S. Grigor'ev and E. Z. Meylikhova (Energoatomizdat, Moscow, 1991).
[28] D. Errandonea, J. Appl. Phys. **108**, 033517 (2010).
[29] D. Errandonea, Phys. Rev. B **87**, 054108 (2013).
[30] J. Jandeleit, G. Urbasch, H. D. Hoffmann, H.-G. Treusch, and E. W. Kreutz, Appl. Phys. A **63**, 117 (1996).
[31] *Handbook of Optical Constants of Solids*, edited by E. D. Palik (Academic Press, Orlando, FL, 1998).
[32] V. I. Emel'yanov and A. S. Kuratov, Eur. Phys. J. B **86**, 381 (2013).
[33] V. I. Emel'yanov, P. A. Danilov, D. A. Zayarny, A. A. Ionin, S. I. Kudryashov, S. V. Makarov, A. A. Rudenko, D. I. Shikunov, and V. I. Yurovskikh, Pis'ma v ZhETF **100**, 163 (2014) [JETP Lett. (to be published)].